V. Franzese, F. Topputo
Optimal Beacons Selection for Deep-Space Optical Navigation
The Journal of the Astronautical Sciences, In press - Published online 10/11/2020
doi:10.1007/s40295-020-00242-z

The Journal of the Astronautical Sciences manuscript No.
(will be inserted by the editor)

Optimal Beacons Selection for Deep-Space Optical Navigation

V. Franzese* · F. Topputo

Received: date / Accepted: date

Abstract Deep-space optical navigation is among the most promising techniques to autonomously estimate the position of a spacecraft in deep space. The method relies on the acquisition of the line-of-sight directions to a number of navigation beacons. The position knowledge depends upon the tracked objects. This paper elaborates on the impact of the observation geometry to the overall performances of the method. A covariance analysis is carried out considering beacons geometry as well as pointing and input errors. A performance index is formulated, and criteria for an optimal beacons selection are derived in a scenario involving two measurements. A test case introducing ten available beacons pairs is used to prove the effectiveness of the developed strategy in selecting the optimal pair, which leads to the smallest achievable error.

Keywords Autonomous Navigation, Optimal Beacons Selection

V. Franzese
*Corresponding author
PhD Candidate, Dept. of Aerospace Science and Technology,
Politecnico di Milano, Via La Masa 34, 20156, Milan, Italy
E-mail: vittorio.franzese@polimi.it

F. Topputo
Associate Professor, Dept. of Aerospace Science and Technology,
Politecnico di Milano, Via La Masa 34, 20156, Milan, Italy,
E-mail: francesco.topputo@polimi.it

1 Introduction

The state of the art for spacecraft navigation is radiometric tracking [24]. The accuracy of the orbit determination solution lies in the order of meters in near-Earth environment whereas it is in the order of kilometers in deep space. This method yields the lowest error achievable with current technology, though it requires persistent contact with ground. Moreover, in two-way communication the orbit determination is performed on ground as well. All in all, radiometric-based orbit determination involves a consistent allocation of resources and assets.

Automation is required for next-generation missions [19]. There is an incoming wave of miniaturized interplanetary probes [18]: the European Space Agency (ESA) has funded several interplanetary CubeSat mission studies like M-ARGO (Miniaturized Asteroid Remote Geophysical Observer) [26], LUMIO (Lunar Meteoroid Impacts Observer) [25,22,7], VMMO (Lunar Volatile and Mineralogy Mapping) [12], and CubeSats along the Hera mission [14]; the National Aeronautics and Space Administration (NASA) funded 19 SmallSat deep-space mission studies after Mars Cube One (MarCO) [11], the first interplanetary CubeSat launched along with InSight (Interior Exploration using Seismic Investigations, Geodesy, and Heat Transport) mission.

Interplanetary CubeSats missions are on the verge of becoming prosperous. Yet, their overall cost scales with the system mass, except for operations [26]. There is therefore the need to reduce operation costs, in particular for what concerns flight-related operations, which are performed incessantly during the entire lifetime. In the field of navigation, the key is to enable autonomous positioning by inferring information from the surrounding environment. Autonomous navigation for deep space missions is thus desirable, in particular for small mission classes.

Navigation schemes are used to determine a spacecraft position, state, or orbit by exploiting some kind of measurements [20]. The navigation with X-ray pulsars compares an incoming pulsar signal to the one predicted in the Solar System Barycenter (SSB) to compute the time-of-arrival difference, thus estimating the range between the spacecraft and the SSB [21,1]. The horizon-based navigation exploits the apparent full-disk of known spherical or nearly ellipsoidal bodies and the attitude knowledge to estimate the spacecraft posi-

tion vector relative to the body [8,16,9,6,4,5]. In deep space, the line-of-sight (LOS) navigation using visible objects exploits the LOS to some bodies for which ephemerides are known to infer the spacecraft position [15,10]. In the frame of the latter method, the error depends on the observation geometry. In particular, since LOS measurements to a pair of celestial bodies are needed to triangulate, questions arise when more than two objects are visible.

Inspired by the LOS navigation mechanism, this work elaborates on the impact of the observation geometry to the overall performances of the method. The aim is to derive the theoretical optimal pair of celestial objects to be tracked as function of a spacecraft trajectory that yields the highest accuracy in the navigation solution. Thus, a real mission scenario including the camera characteristics like the field-of-view and visibility performances is neglected. A covariance analysis is carried out considering beacons geometry as well as pointing and input errors. The optimal pair of beacons stem from the solution of a combinatorial optimization problem. The validity of the approach is discussed by virtue of a test case involving ten available beacons pairs, out of which the optimal pairs are extracted, so yielding to the smallest achievable error. This work complements the results in [2], where similar results were found.

The remainder of the paper is organized as follows. The navigation problem is described in Section 2, the covariance of the navigation solution is derived in Section 3, and the selection criteria is elaborated in Section 4. A test case is discussed in Section 5, whereas final remarks are given in Section 6.

2 The navigation problem

The geometry of a spacecraft that observes two objects in deep-space is shown in Fig. 1. The spacecraft position vector at a given epoch and in a given inertial reference frame is denoted as $\boldsymbol{r}$, which is unknown. The objects positions at the same epoch and in the same frame are denoted as $\boldsymbol{r}_1$ and $\boldsymbol{r}_2$. The relative position vectors of the objects with respect to the observer are denoted as $\boldsymbol{\rho}_1$ and $\boldsymbol{\rho}_2$. The problem is to estimate $\boldsymbol{r}$ by acquiring the LOS directions to the bodies, $\hat{\boldsymbol{\rho}}_1$ and $\hat{\boldsymbol{\rho}}_2$, assuming their ephemeris known; that is, $\boldsymbol{r}_1(t)$ and $\boldsymbol{r}_2(t)$ are known at any time.

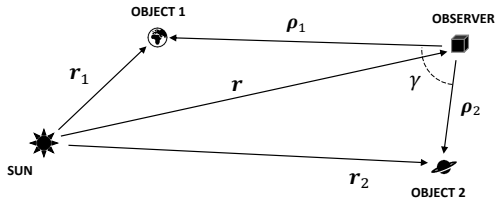

Fig. 1: Line-of-sight navigation exploiting two navigation beacons.

2.1 Solution with exact data

The optical navigation problem with synchronous measurements of two beacons can be solved algebraically. For each object, let $\boldsymbol{\rho} = \rho\hat{\boldsymbol{\rho}}$, ρ and $\hat{\boldsymbol{\rho}}$ being the ranges and the unitary LOS directions, respectively. The latter are assumed exact for now. The ranges $\rho_{1,2}$ to the observed objects can be determined as follows.

From Fig. 1, the observer position can be written as [10]:

$$\boldsymbol{r} = \boldsymbol{r}_1 - \rho_1\,\hat{\boldsymbol{\rho}}_1 \qquad \text{or} \qquad \boldsymbol{r} = \boldsymbol{r}_2 - \rho_2\,\hat{\boldsymbol{\rho}}_2 \tag{1}$$

which leads to

$$\boldsymbol{r}_1 - \rho_1\,\hat{\boldsymbol{\rho}}_1 = \boldsymbol{r}_2 - \rho_2\,\hat{\boldsymbol{\rho}}_2 \tag{2}$$

The scalar product of Eq. (2) by $\hat{\boldsymbol{\rho}}_1$ and $\hat{\boldsymbol{\rho}}_2$, respectively, yields

$$\begin{aligned} \hat{\boldsymbol{\rho}}_1^\top\,\boldsymbol{r}_1 - \rho_1\,\hat{\boldsymbol{\rho}}_1^\top\,\hat{\boldsymbol{\rho}}_1 &= \hat{\boldsymbol{\rho}}_1^\top\,\boldsymbol{r}_2 - \rho_2\,\hat{\boldsymbol{\rho}}_1^\top\,\hat{\boldsymbol{\rho}}_2 \\ \hat{\boldsymbol{\rho}}_2^\top\,\boldsymbol{r}_1 - \rho_1\,\hat{\boldsymbol{\rho}}_2^\top\,\hat{\boldsymbol{\rho}}_1 &= \hat{\boldsymbol{\rho}}_2^\top\,\boldsymbol{r}_2 - \rho_2\,\hat{\boldsymbol{\rho}}_2^\top\,\hat{\boldsymbol{\rho}}_2 \end{aligned} \tag{3}$$

Keeping in mind that $\hat{\boldsymbol{\rho}}_1^\top\,\hat{\boldsymbol{\rho}}_1 = \hat{\boldsymbol{\rho}}_2^\top\,\hat{\boldsymbol{\rho}}_2 = 1$, and rearranging Eq. (3), the following matrix form can be obtained

$$\underbrace{\begin{bmatrix} 1 & -\hat{\boldsymbol{\rho}}_1^\top\,\hat{\boldsymbol{\rho}}_2 \\ -\hat{\boldsymbol{\rho}}_2^\top\,\hat{\boldsymbol{\rho}}_1 & 1 \end{bmatrix}}_{\boldsymbol{A}} \underbrace{\begin{bmatrix} \rho_1 \\ \rho_2 \end{bmatrix}}_{\boldsymbol{x}} = \underbrace{\begin{bmatrix} \hat{\boldsymbol{\rho}}_1^\top\,(\boldsymbol{r}_1 - \boldsymbol{r}_2) \\ \hat{\boldsymbol{\rho}}_2^\top\,(\boldsymbol{r}_2 - \boldsymbol{r}_1) \end{bmatrix}}_{\boldsymbol{b}} \tag{4}$$

Eq. (4) is in the form $\boldsymbol{A}\boldsymbol{x} = \boldsymbol{b}$, where the geometry matrix $\boldsymbol{A}$ and the input vector $\boldsymbol{b}$ are both known: $\hat{\boldsymbol{\rho}}_{1,2}$ are measured directly using star trackers and $\boldsymbol{r}_{1,2}$ are read from ephemeris look-up tables stored on board. The system can be solved for the unknown $\boldsymbol{x} = [\rho_1, \rho_2]^\top$; that is, $\boldsymbol{x} = \boldsymbol{A}^{-1}\,\boldsymbol{b}$. Assuming a perfect measurement (so no errors coming from the sensors), the solution $\boldsymbol{x}$ is

exact. The spacecraft position $\boldsymbol{r}$ is in turn known as well, by using any of Eqs. (1).

However, even under the assumption of exact measurements, the accuracy of the method depends upon the angle between the two LOS directions. Let γ be the angle between the two observed beacons, $\hat{\boldsymbol{\rho}}_1^\top \hat{\boldsymbol{\rho}}_2 = \cos\gamma$, then the geometry matrix can be rewritten as

$$\boldsymbol{A} = \begin{bmatrix} 1 & -\cos\gamma \\ -\cos\gamma & 1 \end{bmatrix} \tag{5}$$

Note that the determinant of $\boldsymbol{A}$ is

$$\det\boldsymbol{A} = 1 - \cos^2\gamma = \sin^2\gamma \tag{6}$$

Thus, the matrix $\boldsymbol{A}$ becomes singular for $\gamma = \{0, \pi\}$ (note that γ is known modulo π). The celestial triangulation is singular when the spacecraft and the two observed objects lie on the same line. On the contrary, $\det\boldsymbol{A} = 1$ for $\gamma = \pi/2$ and $\boldsymbol{A}$ becomes the identity matrix, so that $\boldsymbol{x} = \boldsymbol{b}$.

The same conclusions can be drawn by checking the condition number of $\boldsymbol{A}$, denoted as $\kappa(\boldsymbol{A})$, defined as the ratio of the largest and the smallest singular values of $\boldsymbol{A}$ ($\sigma_{\max}$ and $\sigma_{\min}$, respectively), that is

$$\kappa(\boldsymbol{A}) = \frac{\sigma_{\max}(\boldsymbol{A})}{\sigma_{\min}(\boldsymbol{A})} \tag{7}$$

Note that, for a symmetric matrix, the singular values are equal to the absolute values of the eigenvalues. For $\boldsymbol{A}$ in Eq. (5), the eigenvalues are easily found to be

$$\lambda_1 = 1 + \cos\gamma \qquad\qquad \lambda_2 = 1 - \cos\gamma \tag{8}$$

Note that λ_1 and λ_2 are always non-negative. Thus, for the computation of κ, $\sigma_{\max}(\boldsymbol{A}) = \max\{\lambda_1, \lambda_2\}$, while $\sigma_{\min}(\boldsymbol{A}) = \min\{\lambda_1, \lambda_2\}$. Figure 2 shows the condition number of the geometry matrix $\boldsymbol{A}$ as function of γ. For values of γ approaching 0 or π the problem becomes ill-conditioned ($\det\boldsymbol{A} \to 0$, $\kappa(\boldsymbol{A}) \to +\infty$), while for values of γ approaching $\pi/2$ the problem becomes well-conditioned ($\det\boldsymbol{A} \to 1$, $\kappa(\boldsymbol{A}) \to 1$). Thus, the best posedness of the problem is achieved when the two LOS directions are orthogonal.

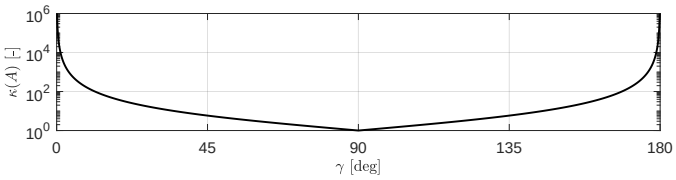

Fig. 2: Condition number of the geometry matrix $\boldsymbol{A}$ as function of γ.

2.2 A simple test case

A simple test case is now considered. A spacecraft is assumed to be on an heliocentric orbit (Fig. 3) whose orbital parameters on the 1st January 2020 are shown in Table 1, where a is the semi-major axis, e the eccentricity, i the inclination, ω the pericenter anomaly, Ω the right ascension of the ascending node, and ν the true anomaly. The values of these parameters have been chosen arbitrarily. During the trajectory, the spacecraft acquires the LOS directions to two beacons, namely the Earth and Mars, without any error associated to the measurements. The planets' trajectories are assumed known and exact. The ideal optical navigation problem can then be solved.

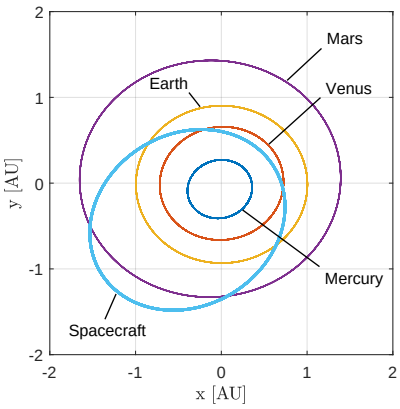

Fig. 3: Spacecraft and planets orbits.

In top plot of Fig. 4, the angle γ is shown as function of the epoch, whereas in the bottom plot the position error norm (left y-axis) and the condition number κ (right y-axis) are reported. The position error is computed as the best case difference between the spacecraft real positions and the spacecraft estimated

Table 1: Spacecraft heliocentric orbital parameters.

a [AU]	e [-]	i [deg]	ω [deg]	Ω [deg]	ν [deg]	Epoch
1.23276	0.50038	25.58506	48.98111	1.23296	129.78597	01 Jan 2020

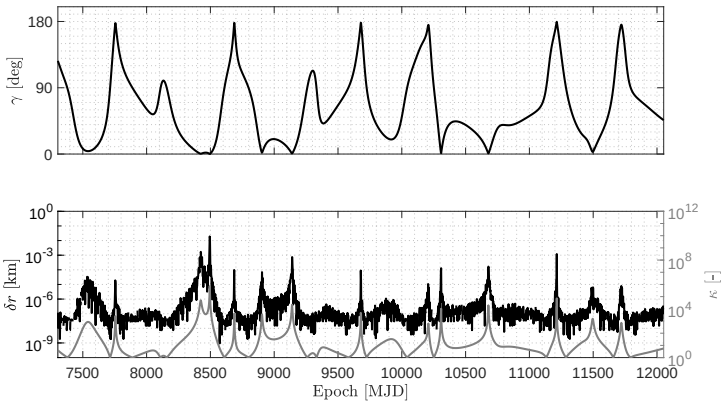

Fig. 4: Angle between beacons γ, position error norm δr, and condition number κ.

positions. Thus,

$$\delta r = \min\{\|\boldsymbol{r} - (\boldsymbol{r}_1 - \rho_1\,\hat{\boldsymbol{\rho}}_1)\|, \|\boldsymbol{r} - (\boldsymbol{r}_2 - \rho_2\,\hat{\boldsymbol{\rho}}_2)\|\} \tag{9}$$

where

$$\rho_1 = \boldsymbol{h}_1\,\boldsymbol{A}^{-1}\boldsymbol{b}, \qquad \rho_2 = \boldsymbol{h}_2\,\boldsymbol{A}^{-1}\boldsymbol{b} \tag{10}$$

and $\boldsymbol{h}_1 = [1\ 0]$, $\boldsymbol{h}_2 = [0\ 1]$.

Inspection of Fig. 4 suggests that under the ideal assumption that the LOS measurements are exact the error in position is always below the meter. Nevertheless, the dependency of the error on γ is clear, since the accuracy of the method for $\gamma = 90$ deg is in the order of 10^{-8} km, while the accuracy for $\gamma = 0$ or 180 deg is in the order of 10^{-3} km. Thus, there is a difference of 5 orders of magnitude in position accuracy albeit with ideal measurements. This feature is ascribable to the geometry. It is remarkable to note that, as expected, δr and κ follow the same trend as function of γ.

2.3 Test case with LOS uncertainty

The line-of-sight directions to the navigation beacons are now assumed known with given confidence. Three different cases are considered where the LOS directions are affected by a white noise having a 3σ standard deviation of 1, 10, and 20 arcseconds, respectively, which is consistent with current technology. Let the exact LOS be

$$\hat{\boldsymbol{\rho}} = [\cos\phi\cos\theta,\, \cos\phi\sin\theta,\, \sin\phi]^\top \tag{11}$$

where θ and ϕ are the nominal azimuth and elevation, respectively. These two angles are perturbed by the white noises $v_\theta \sim \mathcal{N}(0,\, \sigma_L^2)$ and $v_\phi \sim \mathcal{N}(0,\, \sigma_L^2)$ having zero mean and given standard deviation σ_L; that is $\theta^\epsilon = \theta + v_\theta$, $\phi^\epsilon = \phi + v_\phi$. The perturbed LOS direction

$$\hat{\boldsymbol{\rho}} = [\cos\phi^\epsilon\cos\theta^\epsilon,\, \cos\phi^\epsilon\sin\theta^\epsilon,\, \sin\phi^\epsilon]^\top \tag{12}$$

is given as input to Eq. (4) (both to $\boldsymbol{A}$ and $\boldsymbol{b}$) and the solution error δr is evaluated as per Eq. (9). The same orbital geometry in Section 2.2 is considered. Figure 5 shows the performances of the method, where the total error δr is shown on the left y-axis for the three different levels of LOS uncertainty. There are several orders of magnitude difference in δr for the different cases. The total error for the 1 arcsecond case ranges in 10^1–10^4 km, while it grows up to 10^3–10^7 km for the 20 arcseconds case. On the right y-axis, the condition number κ computed with exact γ is reported. Again, it is remarkable to note the same trend between the condition number and the solution error, which stresses the importance of having a good observation geometry in addition to accurate LOS measurements.

2.4 Dependency on γ

The navigation problem with perturbed LOS measurements is now simulated. The time window covers 13 years with a sampling time of 2 days. A total of 100 runs are executed at each time step. Then, the mean error and the 3σ covariance bounds across all the runs are computed. This procedure is repeated for three levels of LOS uncertainty introduced in Section 2.3.

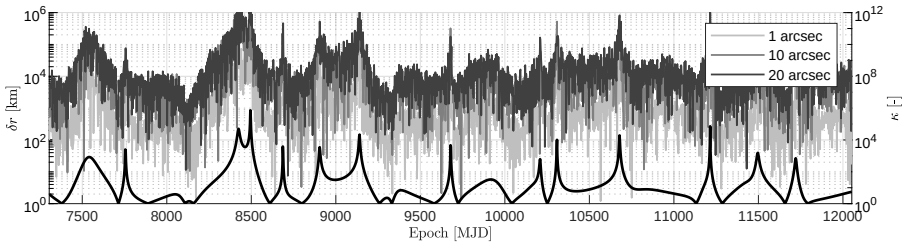

Fig. 5: Total error δr for different levels of LOS uncertainty (1, 10, 20 arcsec) and condition number κ.

The dependency of the total error δr as function of γ for different levels of LOS uncertainty 1, 10, and 20 arcseconds is shown in Fig. 6a, Fig. 6b, and Fig. 6c, respectively. It can be noted that for the two limiting cases of 1 arcseconds and 20 arcseconds, the total error reaches 10^5 and 10^7 km for $\gamma = 0$, respectively, while it is in the order of 10^3 and 10^4 km for $\gamma = 90$ deg. This remarks once again that the accuracy of the method is strongly dependent on the observation geometry. The geometrical considerations drawn for this two beacons case with synchronous measurements apply also to other similar methods with asynchronous measurements.

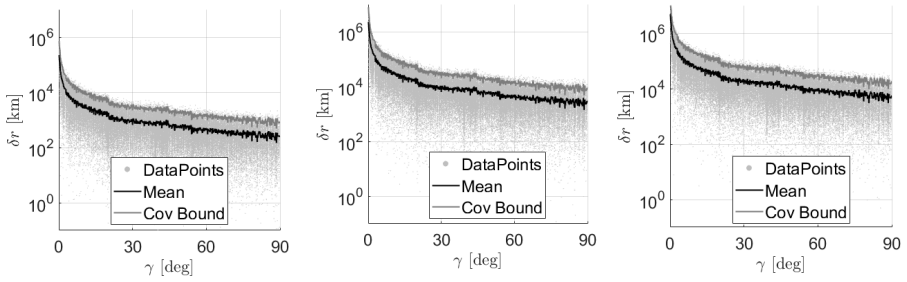

(a) (b) (c)

Fig. 6: Total error δr as function of γ for different LOS uncertainties: (a) 1 arcsec; (b) 10 arcsec; (c) 20 arcsec.

3 Covariance Analysis

The covariance analysis for the deep-space optical navigation problem exploiting two beacons is presented in this section. Eq. (4) is the algebraic system to solve with exact data.

However, the line-of-sight directions $\hat{\boldsymbol{\rho}}_{1,2}$ measured by a sensor (e.g., a star tracker) are affected by errors. Thus, both the input to the system ($\boldsymbol{b}$) and the geometry matrix ($\boldsymbol{A}$) are affected by the errors as well. It is then desirable to estimate the solution error covariance by considering perturbed line-of-sight directions.

3.1 LOS measurement model

In presence of small perturbations, the QUEST measurement model can be used to introduce the errors in the line-of-sight directions [13]. The QUEST measurement model is a linear additive model, thus it considers the perturbed LOS direction as a linear sum of the true line-of-sight with a white noise process. In other words

$$\hat{\boldsymbol{\rho}}^{\epsilon} = \hat{\boldsymbol{\rho}} + \boldsymbol{v} \tag{13}$$

where $\hat{\boldsymbol{\rho}}^{\epsilon}$ is the perturbed LOS direction, $\hat{\boldsymbol{\rho}}$ is the true one, and $\boldsymbol{v}$ is a white-noise process whose components have zero mean and standard deviation σ. Calling E the expected value operator, then [3]

$$\mathrm{E}[\boldsymbol{v}] = \boldsymbol{0} \qquad \mathrm{E}[\boldsymbol{v}\boldsymbol{v}^{\top}] = \sigma^2[\boldsymbol{I} - \hat{\boldsymbol{\rho}}\hat{\boldsymbol{\rho}}^{\top}] \tag{14}$$

Equations (13) and (14) hold for small rotations, where the spherical surface generated by a rotation of the tip of $\hat{\boldsymbol{\rho}}$ is locally approximated by the tangent plane. Thus, $\boldsymbol{v}$ lies on this plane and is orthogonal to $\hat{\boldsymbol{\rho}}$, i.e.,

$$\hat{\boldsymbol{\rho}}^{\top}\boldsymbol{v} = 0 \tag{15}$$

Note that this model alters the unitary norm of the LOS direction, yet it is a good approximation in case of small angles; it is widely used in the literature [3]. In case of large angles, a more accurate multiplicative model shall be used [17].

3.2 Perturbed input

In presence of perturbed LOS directions, the perturbed input to the system is

$$\boldsymbol{b}^{\epsilon} = \boldsymbol{b} + \Delta\boldsymbol{b} \tag{16}$$

where $\boldsymbol{b}^{\epsilon}$ is the perturbed input, $\boldsymbol{b}$ the exact input, and $\Delta\boldsymbol{b}$ the input error. Assuming exact ephemeris data (that is, no errors in $\boldsymbol{r}_1$ and $\boldsymbol{r}_2$), and defining $\boldsymbol{z} = \boldsymbol{r_1} - \boldsymbol{r}_2$, the perturbed input is

$$\boldsymbol{b}^{\epsilon} = \begin{bmatrix} \hat{\boldsymbol{\rho}}_1^{\epsilon\top}\boldsymbol{z} \\ -\hat{\boldsymbol{\rho}}_2^{\epsilon\top}\boldsymbol{z} \end{bmatrix} = \underbrace{\begin{bmatrix} \hat{\boldsymbol{\rho}}_1^{\top} z \\ -\hat{\boldsymbol{\rho}}_2^{\top}\boldsymbol{z} \end{bmatrix}}_{\boldsymbol{b}} + \underbrace{\begin{bmatrix} \boldsymbol{v}_1^{\top}\boldsymbol{z} \\ -\boldsymbol{v}_2^{\top}\boldsymbol{z} \end{bmatrix}}_{\Delta\boldsymbol{b}} \tag{17}$$

3.3 Perturbed geometry matrix

The perturbed geometry matrix $\boldsymbol{A}^{\epsilon}$ is

$$\boldsymbol{A}^{\epsilon} = \begin{bmatrix} 1 & -\hat{\boldsymbol{\rho}}_1^{\epsilon\top}\hat{\boldsymbol{\rho}}_2^{\epsilon} \\ -\hat{\boldsymbol{\rho}}_2^{\epsilon\top}\hat{\boldsymbol{\rho}}_1^{\epsilon} & 1 \end{bmatrix} \tag{18}$$

Note that the off-diagonal terms in $\boldsymbol{A}^{\epsilon}$ can be developed as

$$\hat{\boldsymbol{\rho}}_2^{\epsilon\top}\hat{\boldsymbol{\rho}}_1^{\epsilon} = \hat{\boldsymbol{\rho}}_1^{\epsilon\top}\hat{\boldsymbol{\rho}}_2^{\epsilon} = (\hat{\boldsymbol{\rho}}_1 + \boldsymbol{v}_1)^{\top}(\hat{\boldsymbol{\rho}}_2 + \boldsymbol{v}_2) = \hat{\boldsymbol{\rho}}_1^{\top}\hat{\boldsymbol{\rho}}_2 + \hat{\boldsymbol{\rho}}_1^{\top}\boldsymbol{v}_2 + \boldsymbol{v}_1^{\top}\hat{\boldsymbol{\rho}}_2 + \boldsymbol{v}_1^{\top}\boldsymbol{v}_2 \tag{19}$$

The term $\boldsymbol{v}_1^{\top}\boldsymbol{v}_2$ can be neglected because it is a perturbation of higher order. Thus, let the first-order term be

$$m = \hat{\boldsymbol{\rho}}_1^{\top}\boldsymbol{v}_2 + \boldsymbol{v}_1^{\top}\hat{\boldsymbol{\rho}}_2 \tag{20}$$

Equation (19) can be rewritten as

$$\hat{\boldsymbol{\rho}}_2^{\epsilon\top}\hat{\boldsymbol{\rho}}_1^{\epsilon} = \hat{\boldsymbol{\rho}}_1^{\epsilon\top}\hat{\boldsymbol{\rho}}_2^{\epsilon} \simeq \hat{\boldsymbol{\rho}}_1^{\top}\hat{\boldsymbol{\rho}}_2 + m \tag{21}$$

Note that $\mathrm{E}[m] = 0$ because $\mathrm{E}[\boldsymbol{v}_1] = \mathrm{E}[\boldsymbol{v}_2] = \boldsymbol{0}$. Thus, Eq. (18) can be expanded as

$$\boldsymbol{A}^{\epsilon} = \begin{bmatrix} 1 & -\hat{\boldsymbol{\rho}}_1^{\epsilon\top}\hat{\boldsymbol{\rho}}_2^{\epsilon} \\ -\hat{\boldsymbol{\rho}}_2^{\epsilon\top}\hat{\boldsymbol{\rho}}_1^{\epsilon} & 1 \end{bmatrix} = \underbrace{\begin{bmatrix} 1 & -\hat{\boldsymbol{\rho}}_1^{\top}\hat{\boldsymbol{\rho}}_2 \\ -\hat{\boldsymbol{\rho}}_2^{\top}\hat{\boldsymbol{\rho}}_1 & 1 \end{bmatrix}}_{\boldsymbol{A}} - m\underbrace{\begin{bmatrix} 0 & 1 \\ 1 & 0 \end{bmatrix}}_{\boldsymbol{Y}} \tag{22}$$

In this way, the perturbed geometry matrix can be seen as $\boldsymbol{A}^{\epsilon} = \boldsymbol{A} + \Delta\boldsymbol{A}$ where $\Delta\boldsymbol{A} = -m\boldsymbol{Y}$. Note also that $\mathrm{E}[\boldsymbol{A}^{\epsilon}] = \boldsymbol{A}$ since $\mathrm{E}[m] = 0$.

3.4 Perturbed solution

The perturbed solution of system (4), $\boldsymbol{x}^{\epsilon}$, can now be computed as

$$\boldsymbol{x}^{\epsilon} = \left(\boldsymbol{A}^{\epsilon}\right)^{-1} \boldsymbol{b}^{\epsilon} \tag{23}$$

In presence of small perturbations, the inverse of a perturbed matrix can be approximated as [23]

$$\left(\boldsymbol{A}^{\epsilon}\right)^{-1} = \left(\boldsymbol{A} + \Delta\boldsymbol{A}\right)^{-1} \simeq \boldsymbol{A}^{-1} - \boldsymbol{A}^{-1}\Delta\boldsymbol{A}\,\boldsymbol{A}^{-1} \tag{24}$$

Considering that $\Delta\boldsymbol{A} = -m\boldsymbol{Y}$ (see Eq. (22)), Eq. (24) becomes

$$\left(\boldsymbol{A}^{\epsilon}\right)^{-1} = \boldsymbol{A}^{-1} + m\,\underbrace{\boldsymbol{A}^{-1}\boldsymbol{Y}\,\boldsymbol{A}^{-1}}_{\boldsymbol{M}} = \boldsymbol{A}^{-1} + m\,\boldsymbol{M} \tag{25}$$

Again, note that $\mathrm{E}[\left(\boldsymbol{A}^{\epsilon}\right)^{-1}] = \mathrm{E}[\boldsymbol{A}^{-1}]$ because $\mathrm{E}[m] = 0$. Considering that , through Eq. (5),

$$\boldsymbol{A}^{-1} = \frac{1}{\sin\gamma^2}\begin{bmatrix} 1 & \cos\gamma \\ \cos\gamma & 1 \end{bmatrix} \tag{26}$$

it is easy to derive the expression for $\boldsymbol{M}$ as

$$\boldsymbol{M} = \boldsymbol{A}^{-1}\boldsymbol{Y}\boldsymbol{A}^{-1} = \frac{1}{\sin^4\gamma}\begin{bmatrix} 2\cos\gamma & \cos^2\gamma + 1 \\ \cos^2\gamma + 1 & 2\cos\gamma \end{bmatrix} \tag{27}$$

Now, expanding the perturbed solution as $\boldsymbol{x}^{\epsilon} = \boldsymbol{x} + \Delta\boldsymbol{x}$ where $\Delta\boldsymbol{x}$ is the solution error, Eq. (23) can be written as

$$\boldsymbol{x} + \Delta\boldsymbol{x} = (\boldsymbol{A}^{-1} + m\boldsymbol{M})(\boldsymbol{b} + \Delta\boldsymbol{b}) = \boldsymbol{A}^{-1}\,\boldsymbol{b} + \boldsymbol{A}^{-1}\Delta\boldsymbol{b} + m\boldsymbol{M}\boldsymbol{b} + m\boldsymbol{M}\Delta\boldsymbol{b} \tag{28}$$

Eliminating the exact solution $\boldsymbol{x} = \boldsymbol{A}^{-1}\boldsymbol{b}$ from both sides of Eq. (28) and neglecting the higher order term $m\boldsymbol{M}\Delta\boldsymbol{b}$, the following expression for the solution error is obtained

$$\Delta\boldsymbol{x} = \boldsymbol{A}^{-1}\Delta\boldsymbol{b} + m\boldsymbol{M}\boldsymbol{b} \tag{29}$$

The solution error can thus be seen as a sum of two contributions, one coming from the perturbed part of the input ($\boldsymbol{A}^{-1}\boldsymbol{\Delta b}$) and one coming from the perturbed part of the geometry matrix ($m\boldsymbol{M}\boldsymbol{b}$). Note that $\mathrm{E}[\boldsymbol{\Delta x}] = \mathbf{0}$ since $\mathrm{E}[\boldsymbol{\Delta b}] = \mathbf{0}$ and $\mathrm{E}[m] = 0$.

3.5 Solution covariance

The covariance of the solution error is

$$\boldsymbol{P}_{\boldsymbol{\Delta x}\boldsymbol{\Delta x}} = \mathrm{E}[\boldsymbol{\Delta x}\boldsymbol{\Delta x}^\top] = \underbrace{\boldsymbol{A}^{-1}\mathrm{E}[\boldsymbol{\Delta b}\boldsymbol{\Delta b}^\top]\boldsymbol{A}^{-\top}}_{\boldsymbol{P}_1} + \underbrace{\boldsymbol{M}\boldsymbol{b}\mathrm{E}[m^2]\boldsymbol{b}^\top\boldsymbol{M}^\top}_{\boldsymbol{P}_2} + \underbrace{\boldsymbol{A}^{-1}\mathrm{E}[m\boldsymbol{\Delta b}]\boldsymbol{b}^\top\boldsymbol{M}^\top + \boldsymbol{M}\boldsymbol{b}\mathrm{E}[m\boldsymbol{\Delta b}^\top]\boldsymbol{A}^{-\top}}_{\boldsymbol{P}_3} \tag{30}$$

The three terms composing $\boldsymbol{P}_{\boldsymbol{\Delta x}\boldsymbol{\Delta x}}$ are developed in the following.

3.5.1 Computation of P1

Let

$$\boldsymbol{P}_1 = \boldsymbol{A}^{-1}\mathrm{E}[\boldsymbol{\Delta b}\boldsymbol{\Delta b}^\top]\boldsymbol{A}^{-\top} \tag{31}$$

Keeping in mind that $\boldsymbol{\Delta b} = [\boldsymbol{v}_1^\top\,\boldsymbol{z}\,;\,-\boldsymbol{v}_2^\top\,\boldsymbol{z}]^\top$ and $\boldsymbol{z} = \boldsymbol{r}_1 - \boldsymbol{r}_2$ (see Eq. (16)) the covariance of the input error can be developed as

$$\mathrm{E}[\boldsymbol{\Delta b}\boldsymbol{\Delta b}^\top] = \mathrm{E}\begin{bmatrix} \boldsymbol{z}^\top\boldsymbol{v}_1\boldsymbol{v}_1^\top\boldsymbol{z} & -\boldsymbol{z}^\top\boldsymbol{v}_1\boldsymbol{v}_2^\top\boldsymbol{z} \\ -\boldsymbol{z}^\top\boldsymbol{v}_2\boldsymbol{v}_1^\top\boldsymbol{z} & \boldsymbol{z}^\top\boldsymbol{v}_2\boldsymbol{v}_2^\top\boldsymbol{z} \end{bmatrix} \tag{32}$$

Assuming no errors in the ephemeris, $\mathrm{E}[\boldsymbol{z}] = \boldsymbol{z}$. Then, for uncorrelated processes,

$$\mathrm{E}[\boldsymbol{v}_1\boldsymbol{v}_2^\top] = \mathbf{0} \qquad \mathrm{E}[\boldsymbol{v}_2\boldsymbol{v}_1^\top] = \mathbf{0} \tag{33}$$

Thus, Eq. (32) becomes

$$\mathrm{E}[\boldsymbol{\Delta b}\boldsymbol{\Delta b}^\top] = \begin{bmatrix} \boldsymbol{z}^\top\mathrm{E}[\boldsymbol{v}_1\boldsymbol{v}_1^\top]\,\boldsymbol{z} & 0 \\ 0 & \boldsymbol{z}^\top\mathrm{E}[\boldsymbol{v}_2\boldsymbol{v}_2^\top]\,\boldsymbol{z} \end{bmatrix} \tag{34}$$

Then, plugging Eq. (14) into Eq. (34)

$$\mathrm{E}[\boldsymbol{\Delta b}\boldsymbol{\Delta b}^\top] = \sigma^2 \underbrace{\begin{bmatrix} \boldsymbol{z}^\top\boldsymbol{L}_1\,\boldsymbol{z} & 0 \\ 0 & \boldsymbol{z}^\top\boldsymbol{L}_2\,\boldsymbol{z} \end{bmatrix}}_{\boldsymbol{B}} \tag{35}$$

where

$$\boldsymbol{L}_1 = \boldsymbol{I} - \hat{\boldsymbol{\rho}}_1\hat{\boldsymbol{\rho}}_1^\top \qquad \boldsymbol{L}_2 = \boldsymbol{I} - \hat{\boldsymbol{\rho}}_2\hat{\boldsymbol{\rho}}_2^\top \tag{36}$$

Thus, noting also that $\boldsymbol{A}^{-\top} = \boldsymbol{A}^{-1}$

$$\boldsymbol{P}_1 = \boldsymbol{A}^{-1}\,\mathrm{E}[\Delta\boldsymbol{b}\Delta\boldsymbol{b}^\top]\,\boldsymbol{A}^{-\top} = \sigma^2\boldsymbol{A}^{-1}\boldsymbol{B}\,\boldsymbol{A}^{-1} \tag{37}$$

3.5.2 Computation of P2

The expression for $\boldsymbol{P}_2$ is

$$\boldsymbol{P}_2 = \mathrm{E}[\boldsymbol{M}\boldsymbol{b}m^2\boldsymbol{b}^\top\boldsymbol{M}^\top] = \boldsymbol{M}\boldsymbol{b}\boldsymbol{b}^\top\boldsymbol{M}^\top\mathrm{E}[m^2] \tag{38}$$

Recalling that $m = \hat{\boldsymbol{\rho}}_1^\top\boldsymbol{v}_2 + \boldsymbol{v}_1^\top\hat{\boldsymbol{\rho}}_2$, then

$$m^2 = \hat{\boldsymbol{\rho}}_1^\top\boldsymbol{v}_2\,\boldsymbol{v}_2^\top\hat{\boldsymbol{\rho}}_1 + \hat{\boldsymbol{\rho}}_2^\top\,\boldsymbol{v}_1\boldsymbol{v}_1^\top\hat{\boldsymbol{\rho}}_2 + 2\,\hat{\boldsymbol{\rho}}_1^\top\boldsymbol{v}_2\,\boldsymbol{v}_1^\top\hat{\boldsymbol{\rho}}_2 \tag{39}$$

Considering the properties of $\boldsymbol{v}_1$ and $\boldsymbol{v}_2$ as per Eq. (14) and Eq. (33), and $\boldsymbol{L}_1$ and $\boldsymbol{L}_2$ as per Eq. (36), the expected value of Eq. (39) yields to

$$\mathrm{E}[m^2] = \sigma^2\hat{\boldsymbol{\rho}}_1^\top\boldsymbol{L}_2\,\hat{\boldsymbol{\rho}}_1 + \sigma^2\hat{\boldsymbol{\rho}}_2^\top\boldsymbol{L}_1\,\hat{\boldsymbol{\rho}}_2 \tag{40}$$

Keeping in mind that $\hat{\boldsymbol{\rho}}_1^\top\hat{\boldsymbol{\rho}}_1 = \hat{\boldsymbol{\rho}}_2^\top\hat{\boldsymbol{\rho}}_2 = 1$ and $\hat{\boldsymbol{\rho}}_1^\top\hat{\boldsymbol{\rho}}_2 = \hat{\boldsymbol{\rho}}_2^\top\hat{\boldsymbol{\rho}}_1 = \cos\gamma$, it is easy to verify that

$$\hat{\boldsymbol{\rho}}_1^\top\boldsymbol{L}_2\,\hat{\boldsymbol{\rho}}_1 = \hat{\boldsymbol{\rho}}_1^\top\hat{\boldsymbol{\rho}}_1 - \hat{\boldsymbol{\rho}}_1^\top\hat{\boldsymbol{\rho}}_2\,\hat{\boldsymbol{\rho}}_2^\top\hat{\boldsymbol{\rho}}_1 = 1 - \cos^2\gamma \tag{41}$$

$$\hat{\boldsymbol{\rho}}_2^\top\boldsymbol{L}_1\,\hat{\boldsymbol{\rho}}_2 = \hat{\boldsymbol{\rho}}_2^\top\hat{\boldsymbol{\rho}}_2 - \hat{\boldsymbol{\rho}}_2^\top\hat{\boldsymbol{\rho}}_1\,\hat{\boldsymbol{\rho}}_1^\top\hat{\boldsymbol{\rho}}_2 = 1 - \cos^2\gamma \tag{42}$$

Thus, the expected value of m^2 can be simply obtained as

$$\mathrm{E}[m^2] = \sigma^2(1-\cos^2\gamma) + \sigma^2(1-\cos^2\gamma) = 2\,\sigma^2\sin^2\gamma \tag{43}$$

Thus

$$\boldsymbol{P}_2 = 2\,\sigma^2\sin^2\gamma\,\boldsymbol{M}\boldsymbol{b}\boldsymbol{b}^\top\boldsymbol{M}^\top \tag{44}$$

3.5.3 Computation of P3

The expression for $\boldsymbol{P}_3$ is

$$\boldsymbol{P}_3 = \boldsymbol{A}^{-1}\mathrm{E}[m\Delta\boldsymbol{b}]\boldsymbol{b}^\top\boldsymbol{M}^\top + \boldsymbol{M}\boldsymbol{b}\,\mathrm{E}[m\Delta\boldsymbol{b}^\top]\boldsymbol{A}^{-\top} \tag{45}$$

Noting that

$$m\Delta\boldsymbol{b} = (\hat{\boldsymbol{\rho}}_1^\top\boldsymbol{v}_2 + \hat{\boldsymbol{\rho}}_2^\top\boldsymbol{v}_1)\begin{bmatrix}\boldsymbol{v}_1^\top\boldsymbol{z}\\ -\boldsymbol{v}_2^\top\boldsymbol{z}\end{bmatrix} \tag{46}$$

It can be verified that

$$\mathrm{E}[m\Delta\boldsymbol{b}] = \begin{bmatrix} \hat{\boldsymbol{\rho}}_2^\top \mathrm{E}[\boldsymbol{v}_1\boldsymbol{v}_1^\top]\,\boldsymbol{z} \\ -\hat{\boldsymbol{\rho}}_1^\top \mathrm{E}[\boldsymbol{v}_2\boldsymbol{v}_2^\top]\,\boldsymbol{z} \end{bmatrix} = \sigma^2 \underbrace{\begin{bmatrix} \hat{\boldsymbol{\rho}}_2^\top \boldsymbol{L}_1\,\boldsymbol{z} \\ -\hat{\boldsymbol{\rho}}_1^\top \boldsymbol{L}_2\,\boldsymbol{z} \end{bmatrix}}_{\boldsymbol{c}} = \sigma^2 \boldsymbol{c} \tag{47}$$

Note that $\boldsymbol{c}$ can be further developed as

$$\boldsymbol{c} = \begin{bmatrix} \hat{\boldsymbol{\rho}}_2^\top \boldsymbol{L}_1\,\boldsymbol{z} \\ -\hat{\boldsymbol{\rho}}_1^\top \boldsymbol{L}_2\,\boldsymbol{z} \end{bmatrix} = \begin{bmatrix} \hat{\boldsymbol{\rho}}_2^\top \boldsymbol{z} - \cos\gamma \hat{\boldsymbol{\rho}}_1^\top \boldsymbol{z} \\ -\hat{\boldsymbol{\rho}}_1^\top \boldsymbol{z} + \cos\gamma \hat{\boldsymbol{\rho}}_2^\top \boldsymbol{z} \end{bmatrix} = \begin{bmatrix} -\cos\gamma & -1 \\ -1 & -\cos\gamma \end{bmatrix} \begin{bmatrix} \hat{\boldsymbol{\rho}}_1^\top \boldsymbol{z} \\ -\hat{\boldsymbol{\rho}}_2^\top \boldsymbol{z} \end{bmatrix} = -\underbrace{\begin{bmatrix} 0 & 1 \\ 1 & 0 \end{bmatrix}}_{\boldsymbol{Y}} \underbrace{\begin{bmatrix} 1 & \cos\gamma \\ \cos\gamma & 1 \end{bmatrix}}_{\sin^2\gamma\,\boldsymbol{A}^{-1}} \underbrace{\begin{bmatrix} \hat{\boldsymbol{\rho}}_1^\top \boldsymbol{z} \\ -\hat{\boldsymbol{\rho}}_2^\top \boldsymbol{z} \end{bmatrix}}_{\boldsymbol{b}} \tag{48}$$

Thus

$$\mathrm{E}[m\Delta\boldsymbol{b}] = -\sigma^2 \sin^2\gamma\, \boldsymbol{Y}\boldsymbol{A}^{-1}\boldsymbol{b} \tag{49}$$

So, keeping in mind that $\boldsymbol{M} = \boldsymbol{A}^{-1}\boldsymbol{Y}\boldsymbol{A}^{-1}$ and noting that $\boldsymbol{M} = \boldsymbol{M}^\top$, $\boldsymbol{P}_3$ can be developed as

$$\begin{aligned} \boldsymbol{P}_3 =& \boldsymbol{A}^{-1}\mathrm{E}[m\Delta\boldsymbol{b}]\boldsymbol{b}^\top\boldsymbol{M}^\top + \boldsymbol{M}\boldsymbol{b}\,\mathrm{E}[m\Delta\boldsymbol{b}^\top]\boldsymbol{A}^{-\top} \\ =& -\sigma^2 \sin^2\gamma\, \underbrace{\boldsymbol{A}^{-1}\boldsymbol{Y}\boldsymbol{A}^{-1}}_{\boldsymbol{M}} \boldsymbol{b}\boldsymbol{b}^\top\boldsymbol{M}^\top - \sigma^2 \sin^2\gamma\, \boldsymbol{M}\boldsymbol{b}\boldsymbol{b}^\top \underbrace{\boldsymbol{A}^{-\top}\boldsymbol{Y}^\top\boldsymbol{A}^{-\top}}_{\boldsymbol{M}^\top} \\ =& -2\sigma^2 \sin^2\gamma\, \boldsymbol{M}\boldsymbol{b}\boldsymbol{b}^\top\boldsymbol{M}^\top \end{aligned} \tag{50}$$

And, recalling Eq. (44), it can be noted that

$$\boldsymbol{P}_3 = -\boldsymbol{P}_2 \tag{51}$$

So, the covariance of the solution error is

$$\boldsymbol{P}_{\Delta\boldsymbol{x}\Delta\boldsymbol{x}} = \boldsymbol{P}_1 + \underbrace{\boldsymbol{P}_2 + \boldsymbol{P}_3}_{=\boldsymbol{0}} = \sigma^2 \boldsymbol{A}^{-1}\boldsymbol{B}\,\boldsymbol{A}^{-1} \tag{52}$$

4 Optimal Beacons Selection

This section features the derivation of a figure of merit for deep-space optical navigation. The goal is to find the optimal pair of beacons to track among all the available ones. Figure 7 shows a three beacons scenario, where $\boldsymbol{r}_{1,2,3}$ denote the objects inertial positions, $\boldsymbol{\rho}_{1,2,3}$ the objects positions with respect to the observer, and γ_{12}, γ_{13}, and γ_{23} the angles between the beacons as seen from the observer. In presence of three beacons, there are three possible

pairs to be exploited for optical navigation. Each pair of beacons will yield a different navigation solution accuracy owing to the problem geometry. Thus, the optimal beacons selection aims to determine the pair of beacons that yield the best accuracy of the navigation solution. This is done by exploiting the solution error covariance matrix derived in Section 3.

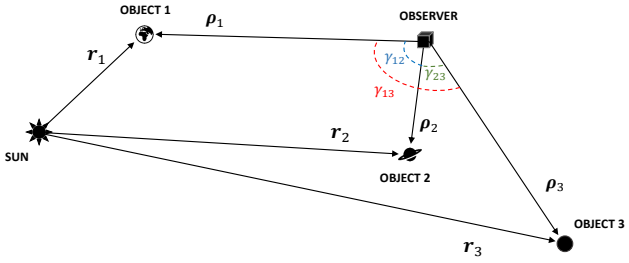

Fig. 7: Optical navigation scenario with multiple beacons.

4.1 Trace of the covariance matrix

Since $\Delta\boldsymbol{x} = [\Delta\rho_1\ \Delta\rho_2]^\top$, the covariance of the solution error is

$$\boldsymbol{P}_{\Delta\boldsymbol{x}\Delta\boldsymbol{x}} = \begin{bmatrix} E[\Delta\rho_1\Delta\rho_1] & E[\Delta\rho_1\Delta\rho_2] \\ E[\Delta\rho_2\Delta\rho_1] & E[\Delta\rho_2\Delta\rho_2] \end{bmatrix} \tag{53}$$

where $\Delta\rho_1$ and $\Delta\rho_2$ are the errors in the range estimation to the beacons as function of the LOS error uncertainty σ, the angle between beacons γ, the geometry of the beacons ($\boldsymbol{r}_1$ and $\boldsymbol{r}_2$), and the line-of-sight directions to the beacons ($\hat{\boldsymbol{\rho}}_1$ and $\hat{\boldsymbol{\rho}}_2$); see Eq. (52). The trace of $\boldsymbol{P}_{\Delta\boldsymbol{x}\Delta\boldsymbol{x}}$,

$$\mathrm{Tr}[\boldsymbol{P}_{\Delta\boldsymbol{x}\Delta\boldsymbol{x}}] = E[\Delta\rho_1^2] + E[\Delta\rho_2^2] \tag{54}$$

is a good indicator of the solution accuracy, and its expression is easily derived in the following.

Starting from Eq. (52), where $\boldsymbol{A}^{-1}$ and $\boldsymbol{B}$ have been defined in Eq. (26) and Eq. (35), respectively, $\boldsymbol{P}_{\Delta\boldsymbol{x}\Delta\boldsymbol{x}}$ can be expanded as

$$\boldsymbol{P}_{\Delta\boldsymbol{x}\Delta\boldsymbol{x}} = \frac{\sigma^2}{\sin^4\gamma} \begin{bmatrix} \boldsymbol{z}^\top(\boldsymbol{L}_1 + \cos^2\gamma\,\boldsymbol{L}_2)\,\boldsymbol{z} & \cos\gamma\,\boldsymbol{z}^\top(\boldsymbol{L}_1 + \boldsymbol{L}_2)\,\boldsymbol{z}) \\ \cos\gamma\,\boldsymbol{z}^\top(\boldsymbol{L}_1 + \boldsymbol{L}_2)\,\boldsymbol{z} & \boldsymbol{z}^\top(\cos^2\gamma\,\boldsymbol{L}_1 + \boldsymbol{L}_2)\,\boldsymbol{z} \end{bmatrix} \tag{55}$$

and therefore

$$\mathrm{Tr}[\boldsymbol{P}_{\Delta\boldsymbol{x}\Delta\boldsymbol{x}}] = \frac{\sigma^2}{\sin^4\gamma}\,\boldsymbol{z}^\top(\boldsymbol{L}_1 + \cos^2\gamma\,\boldsymbol{L}_2 + \cos^2\gamma\,\boldsymbol{L}_1 + \boldsymbol{L}_2)\,\boldsymbol{z} \tag{56}$$

Thus, defining $\boldsymbol{L} = \boldsymbol{L}_1 + \boldsymbol{L}_2$, Eq. (56) can be put in a more compact and elegant form as

$$\mathrm{Tr}[\boldsymbol{P}_{\Delta\boldsymbol{x}\Delta\boldsymbol{x}}] = \sigma^2\,\frac{1+\cos^2\gamma}{\sin^4\gamma}\,\boldsymbol{z}^\top\boldsymbol{L}\,\boldsymbol{z} \tag{57}$$

Note that Eq. (57) is function of the LOS error uncertainty σ, the angle between beacons γ, the positions of the beacons ($\boldsymbol{r}_1$ and $\boldsymbol{r}_2$ inside $\boldsymbol{z}$), and the line-of-sight directions to the beacons ($\hat{\boldsymbol{\rho}}_1$ and $\hat{\boldsymbol{\rho}}_2$ inside $\boldsymbol{L}$). Equation (57) can be used to measure the quality of the navigation solution, it being an always non-negative function of all the quantities and errors involved in the deep-space optical navigation problem.

4.2 Figure of merit

Following the rationale of Eq. (57), the figure of merit for two-beacon, deep-space navigation can be defined as

$$J_{kl} = \sigma^2\left(\frac{1+\cos^2\gamma_{kl}}{\sin^4\gamma_{kl}}\right)(\boldsymbol{r}_l - \boldsymbol{r}_k)^\top[\boldsymbol{L}_k + \boldsymbol{L}_l](\boldsymbol{r}_l - \boldsymbol{r}_k) \tag{58}$$

where k and l denote the k-esimal and l-esimal beacon, respectively, σ the angular error associated to the LOS measurements, γ_{kl} the angle between them as seen from the observer, $\boldsymbol{r}_k$ and $\boldsymbol{r}_l$ their position vector with respect to the Sun, and $\boldsymbol{L}_k = [\boldsymbol{I} - \hat{\boldsymbol{\rho}}_k\hat{\boldsymbol{\rho}}_k^\top]$ and $\boldsymbol{L}_l = [\boldsymbol{I} - \hat{\boldsymbol{\rho}}_l\hat{\boldsymbol{\rho}}_l^\top]$. A similar solution has been derived in [2].

Given a set of N visible beacons, the problem consists in finding those two yielding J_{kl} minimum. This is a combinatorial optimization problem. That is, the problem is to find $i \in \{1,\ldots,N\}$ and $j \in \{1,\ldots,N\}$, $i \neq j$, such that J_{ij} is the minimum among all the possible combinations J_{kl}. More compactly

$$J_{ij} = \min_{\substack{k=1,\cdots,N\\ l=1,\cdots,N\\ k\neq l}} J_{kl} \tag{59}$$

Note that the combinatorial optimization problem in Eq. (59) is to be solved every time a measurement is made.

5 Test Case

The example in Table 1 is now considered as test case to assess the optimal couples of beacons to be tracked during the deep-space travel. For simplicity, only the planets are considered as beacons. The line-of-sight measurements are assumed to be affected by a white noise of 10 arcseconds in 3σ confidence.

Figure 8 shows the navigation error δr and the figure of merit J_{kl} (shown simply as J) for all the possible pairs of beacons exploiting Mercury, Venus, Earth, Mars, and Jupiter during the spacecraft deep-space travel. Note that the error δr and the figure of merit J follow the same trend for all the possible configurations. Sun exclusion angles are neglected as the focus is on beacons geometry.

Solving problem (59) yields the optimal pairs of beacons to track at each time instant. This solution is shown in Figure 9b where the black stripes are the tracking windows. Figure 9a shows the error δr and the figure of merit trend J obtained exploiting the optimal beacons. In practice, the J_{kl} for each couple made up of the planet k and the planet l is evaluated, and then the minimum among all the possible combinations J_{kl} is obtained (Eq. (59)). In this way, the planets corresponding to the minimum J_{kl} are used to solve for the spacecraft position, and the corresponding navigation error is computed. Thus, the error in Figure 9a is derived exploiting always a different couple of beacons, according to the selection in Figure 9b.

For the example in Table 1, it is worth to note that the combinations involving Jupiter are rarely optimal (see the Mar-Jup, Ear-Jup, Ven-Jup, and Mer-Jup options in Figure 9b): Jupiter being far with respect to the spacecraft trajectory, it amplifies the error due to the pointing. The pairs involving Mercury and Mars are ones mostly used.

Table 2 reports the mean error and the standard deviation for the navigation solutions exploiting all the couples of beacons. The last row of the table shows the results for the optimal beacons selection case. It can be seen that, exploiting the optimal beacons selection case, the mean error and the standard deviation of the navigation solutions are at least one order of magnitude lower than all the other cases. To help visualize the data, Figure 10a shows the mean error and 10b shows the standard deviation for all the aforementioned cases.

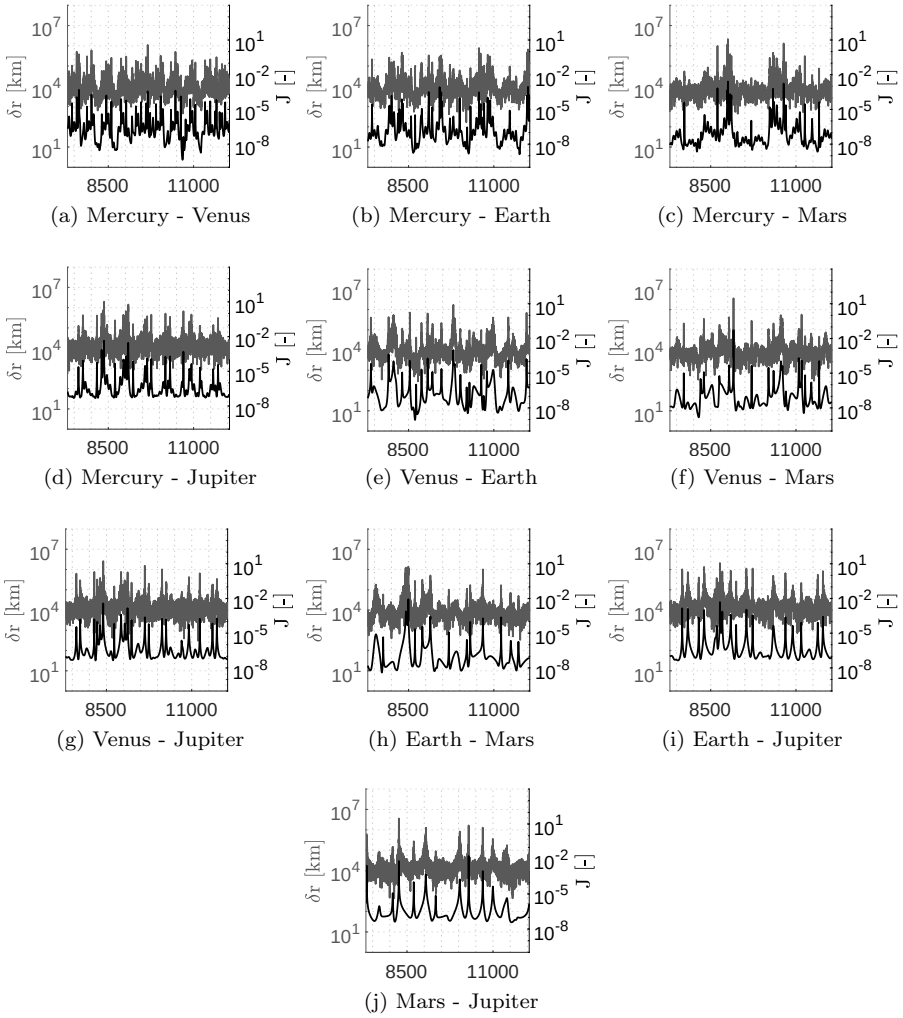

(a) Mercury - Venus (b) Mercury - Earth (c) Mercury - Mars

(d) Mercury - Jupiter (e) Venus - Earth (f) Venus - Mars

(g) Venus - Jupiter (h) Earth - Mars (i) Earth - Jupiter

(j) Mars - Jupiter

Fig. 8: Accuracy of triangulation method (left axis) and figure of merit (right axis) exploiting different pair of beacons during the spacecraft trajectory (the x-axis is Epoch in MJD). The faded lines correspond to δ_r while the black lines correspond to the figure of merit J.

6 Conclusions

In this paper, the impact of the observation geometry to the deep-space navigation solution accuracy has been assessed, and an optimal beacons selection criteria has been derived. The selection criteria has been tested under a

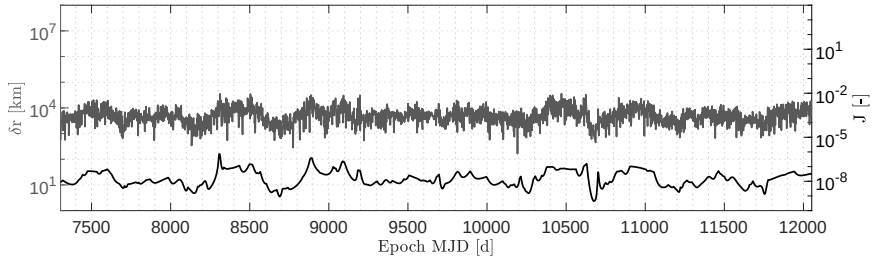

(a) Navigation error (left y-axis) and figure of merit (right y-axis). The faded lines correspond to δ_r while the black lines correspond to the figure of merit J.

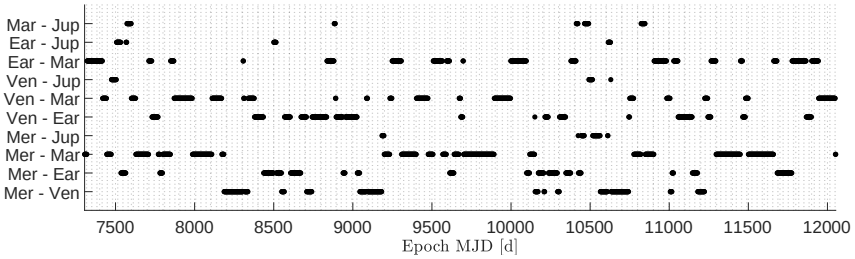

(b) Optimal beacons tracking windows.

Fig. 9: Accuracy of the deep-space optical navigation exploiting the optimal beacons selection.

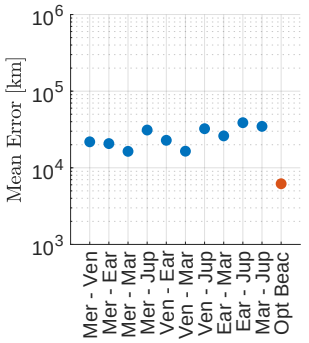

(a) Mean navigation error

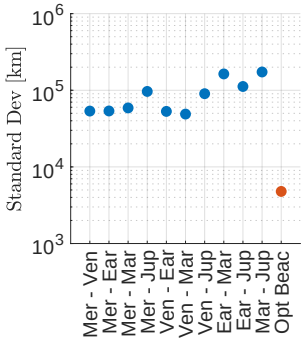

(b) Standard deviation

Fig. 10: Mean navigation error (a) and standard deviation (b) exploiting pairs of navigation beacons.

Table 2: Mean error and standard deviation of deep-space optical navigation with given pairs of beacons (rows 1–10)) and optimal beacons strategy (row 11).

	Mean Error [10^4 km]	**Std. Dev.** [10^5 km]
Mercury–Venus	2.2310	0.5223
Mercury–Earth	2.0987	0.5193
Mercury–Mars	1.9735	0.6413
Mercury–Jupiter	3.5412	1.1346
Venus–Earth	2.4138	0.5347
Venus–Mars	1.8924	0.5811
Venus–Jupiter	3.4819	0.9693
Earth–Mars	2.9473	1.8041
Earth–Jupiter	4.2104	1.1863
Mars–Jupiter	3.4301	1.8850
Optimal Beacons	**0.6665**	**0.0506**

representative deep-space spacecraft trajectory exploiting different couples of planets. The corresponding performances of the deep-space navigation solution have been reported showing the quality of the selection criteria in predicting the accuracy of the navigation solution. This criteria is meant to be the guide for beacons selection in more elaborated navigation schemes (e.g., Kalman filtering).

Acknowledgments

Part of the work presented in this paper has been conducted under ESA Contract No. 4000123920/18/NL/MH.

Conflict of interest

The authors declare that they have no conflict of interest.

References

1. Anderson, K., Pines, D., Sheikh, S.: Validation of pulsar phase tracking for spacecraft navigation. Journal of Guidance, Control, and Dynamics **38**(10), 1885–1897 (2015). doi:10.2514/1.G000789

2. Broschart, S.B., Bradley, N., Bhaskaran, S.: Kinematic approximation of position accuracy achieved using optical observations of distant asteroids. Journal of Spacecraft and Rockets **56**(5), 1383–1392 (2019). doi:10.2514/1.A34354
3. Cheng, Y., Crassidis, J.L., Markley, F.L.: Attitude estimation for large field-of-view sensors. The Journal of the Astronautical Sciences **54**(3-4), 433–448 (2006). doi:10.1007/BF03256499
4. Christian, J.A.: Optical Navigation Using Iterative Horizon Reprojection. Journal of Guidance, Control, and Dynamics **39**(5), 1092–1103 (2016). doi:10.2514/1.G001569
5. Christian, J.A.: Accurate planetary limb localization for image-based spacecraft navigation. Journal of Spacecraft and Rockets **54**(3), 708–730 (2017). doi:10.2514/1.A33692
6. Christian, J.A., Robinson, S.B.: Noniterative Horizon-Based Optical Navigation by Cholesky Factorization. Journal of Guidance, Control, and Dynamics **39**(12), 2757–2765 (2016). doi:10.2514/1.G000539
7. Cipriano, A., Dei Tos, D.A., Topputo, F., et al.: Orbit design for lumio: The lunar meteoroid impacts observer. Frontiers in Astronomy and Space Sciences **5**, 1–29 (2018). doi:10.3389/fspas.2018.00029
8. Franzese, V., Di Lizia, P., Topputo, F.: Autonomous optical navigation for the lunar meteoroid impacts observer. Journal of Guidance, Control, and Dynamics **42**(7), 1579–1586 (2019). doi:10.2514/1.G003999
9. Holt, G.N., D'Souza, C.N., Saley, D.W.: Orion optical navigation progress toward exploration mission 1. In: 2018 Space Flight Mechanics Meeting, AIAA SciTech Forum, pp. 1–12 (2018). doi:10.2514/6.2018-1978
10. Karimi, R., Mortari, D.: Interplanetary Autonomous Navigation Using Visible Planets. Journal of Guidance, Control, and Dynamics **38**(6), 1151–1156 (2015). doi:10.2514/1.G000575
11. Klesh, A., Krajewski, J.: Marco: Cubesats to mars in 2016. In: 29th Annual AIAA/USU Conference on Small Satellites, pp. 1–7 (Logan, UT, 2015)
12. Kruzelecky, R.: VMMO Lunar Volatile and Mineralogy Mapping 12U Cubesat. In: 42nd COSPAR Scientific Assembly, *COSPAR Meeting*, vol. 42, pp. B3.1–6–18 (Pasadena, California, 2018)
13. Markley, F.L., Crassidis, J.L.: Fundamentals of spacecraft attitude determination and control, vol. 33. Springer (2014). Chap. 5
14. Michel, P., Küppers, M., Carnelli, I.: The Hera mission: European component of the ESA-NASA AIDA mission to a binary asteroid. In: 42nd COSPAR Scientific Assembly, *COSPAR Meeting*, vol. 42, pp. 1–42 (Pasadena, California, 2018)
15. Mortari, D., Conway, D.: Single-point position estimation in interplanetary trajectories using star trackers. Advances in the Astronautical Sciences **156**(1), 1909–1926 (2016). doi:10.1007/s10569-016-9738-4
16. Mortari, D., D'Souza, C.N., Zanetti, R.: Image processing of illuminated ellipsoid. Journal of Spacecraft and Rockets pp. 448–456 (2016). doi:10.2514/1.A33342
17. Mortari, D., Majji, M.: Multiplicative measurement model. The Journal of the Astronautical Sciences **57**(1-2), 47–60 (2009). doi:10.1007/BF03321493
18. Poghosyan, A., Golkar, A.: Cubesat evolution: Analyzing cubesat capabilities for conducting science missions. Progress in Aerospace Sciences **88**, 59–83 (2017). doi:10.1016/j.paerosci.2016.11.002
19. Quadrelli, M., Wood, L., Riedel, J.E., McHenry, C.M., Aung, M., Cangahuala, L.A., Volpe, R.A., Beauchamp, P.M., Cutts, J.A.: Guidance, navigation, and control technol-

ogy assessment for future planetary science missions. Journal of Guidance, Control, and Dynamics **38**(7), 1165–1186 (2015). doi:10.2514/1.G000525

20. Schutz, B., Tapley, B., Born, G.H.: Statistical orbit determination, chap. 4, p. 154. Elsevier (2004)
21. Sheikh, S.I., Pines, D.J., Ray, P.S., Wood, K.S., Lovellette, M.N., Wolff, M.T.: Spacecraft Navigation Using X-Ray Pulsars. Journal of Guidance, Control, and Dynamics **29**(1), 49–63 (2006). doi:10.2514/1.13331
22. Speretta, S., Cervone, A., Sundaramoorthy, P., Noomen, R., Mestry, S., Cipriano, A., Topputo, F., Biggs, J., Di Lizia, P., Massari, M., Mani, K.V., Dei Tos, D.A., Ceccherini, S., Franzese, V., Ivanov, A., Labate, D., Tommasi, L., Jochemsen, A., Gailis, J., Furfaro, R., Reddy, V., Vennekens, J., Walker, R.: LUMIO: An Autonomous CubeSat for Lunar Exploration, chap. 6, pp. 103–134. Springer International Publishing (2019). doi:10.1007/978-3-030-11536-4_6
23. Stewart, G.W., Sun, J.g.: Matrix perturbation theory, chap. 3, pp. 130–131. Elsevier Science Publishing Co Inc, Academic Press Inc (1990)
24. Thornton, C.L., Border, J.S.: Radiometric Tracking Techniques for Deep Space Navigation, chap. 2, pp. 9–37. John Wiley & Sons (2003). doi:10.1002/0471728454
25. Topputo, F., Massari, M., Biggs, J., Di Lizia, P., Dei Tos, D., Mani, K., Ceccherini, S., Franzese, V., Cervone, A., Sundaramoorthy, P., et al.: Lumio: a cubesat at earth-moon l2. In: 4S Symposium, pp. 1–15 (Sorrento, 2018)
26. Walker, R., Binns, D., Bramanti, C., Casasco, M., Concari, P., Izzo, D., Feili, D., Fernandez, P., Fernandez, J.G., Hager, P., Koschny, D., Pesquita, V., Wallace, N., Carnelli, I., Khan, M., Scoubeau, M., Taubert, D.: Deep-space cubesats: thinking inside the box. Astronomy & Geophysics **59**(5), 5–24 (2018). doi:10.1093/astrogeo/aty237